Magnetic field control of insulator-metal crossover in cobaltite films via thermally activated percolation

Meng Wang ⬤,[1,*] Keisuke Matsuura ⬤,[1] Masao Nakamura ⬤,[1] Masahiro Sawada,[2]
Masashi Kawasaki,[1,3] and Fumitaka Kagawa ⬤[1,3]

[1]*RIKEN Center for Emergent Matter Science (CEMS), Wako 351-0198, Japan*
[2]*Hiroshima Synchrotron Radiation Center, Hiroshima University, Higashihiroshima, Hiroshima 739-0046, Japan*
[3]*Department of Applied Physics and Quantum-Phase Electronics Center (QPEC), University of Tokyo, Tokyo 113-8656, Japan*

Competition between the double-exchange hopping and Coulomb repulsion underlies fertile phenomena in mixed-valent manganites, such as colossal magnetoresistance associated with a magnetic-field-driven insulator-metal transition (IMT). In contrast, an analogous double-exchange system, perovskite cobaltites, however, shows much smaller magnetoresistance, and the insulator-to-metal phase evolution with field stimulus remains elusive. Here, we unveil a submicrometer-scale phase separation and magnetic-field-controlled crossoverlike IMT in a tensile-strained $La_{0.7}Sr_{0.3}CoO_3$ film. Our transport, magnetization, and magnetic-force-microscopy measurements reveal that, although the IMT is barely induced under an isothermal field sweep, it emerges under field cooling through a thermally activated ferromagnetic domain percolation. Such thermodynamic-history-dependent properties signify a nonergodic feature associated with the microscopic phase separation. By further comparing the transport properties among $La_{0.7}AE_{0.3}CoO_3$ films with AE from Ca, Sr, to Ba, we reveal that the nonergodic behavior prevails in these films and that the mixed spin states are a key factor to enhance the energy barrier for domain-wall motions during domain percolation. Such a spin-state degree of freedom is absent in manganites, probably resulting in the large difference of the phase evolution kinetics in the magnetic-field-induced IMT between cobaltites and manganites.

I. INTRODUCTION

Comparison among materials with analogous orbital configurations is often helpful to clarify the underlying mechanisms for the emergent phenomena. Mixed-valent manganites and cobaltites are typical cases, with a double-exchange interaction and strong coupling effect among charge, spin, lattice, and orbital degrees of freedom, however, presenting distinct differences in magnetic responses [1–4]. In manganites that consist of Mn^{3+} and Mn^{4+} [4–12], Coulombic interactions and electron-lattice coupling favor the charge-orbital-ordered antiferromagnetic-insulator (AFM-I) phase, whereas the double-exchange interaction mediated by the e_g electrons [Fig. 1(a)] favors the ferromagnetic-metal (FM-M) phase [9–10]. These two ordered phases compete at the ground state, and a magnetic field H can thus be a phase-control parameter that stabilizes the metallic phase [Fig. 1(b)]. This magnetic-field-induced first-order transition is inevitably accompanied by a steep decrease in resistivity ρ, representing a phenomenon often referred to as colossal magnetoresistance (CMR) [9–12]. In addition, at the insulator-metal (I-M) phase boundary, the two phases can sometimes coexist in real space despite homogeneous chemical doping and show a percolative feature with a magnetic field stimulus [4,5,8].

Compared with manganites, mixed-valent cobaltites have also been proven to be double-exchange systems, however, with more complexity [Fig. 1(c)] [13–16]. Due to the competition between the crystal field and Hund's rule, the spin states of Co ions can be high spin (HS), intermediate spin (IS), or low spin (LS) depending on the compounds, lattice, and temperature [14]. In $La_{1-x}Sr_xCoO_3$ (LSCO), for instance, authors of previous studies reveal that, as the hole-doping amount x increases, the ground state changes from an insulating state with negligible spontaneous magnetization to a FM-M state, being accompanied by a LS-to-HS transition and a disappearance of the Jahn-Teller distortion [17–21]. More recent experiments further confirm the FM-M state is mainly ascribed to the double-exchange mediated by t_{2g} electrons of $HS-Co^{3+}$ and $HS-Co^{4+}$ ions, while the ratio of $LS-Co^{3+}$ remains low [Fig. 1(c)] [14–16]. One of the macroscopic manifestations of this complexity is that the magnetoresistance (MR) in cobaltites near the I-M phase boundary is much smaller than that in manganites [19,20,22] (the maximum value of $[\rho(H) - \rho(H = 0)]/\rho(H)$ is $\approx -90\%$ at 9 T and 2 K, in contrast to seven orders of magnitude in $Pr_{0.65}Ca_{0.35}MnO_3$ [12]). Additionally, although the phase separation of non-FM-I and FM-M in bulk LSCO has been reported [23,24], a magnetic-field-controlled percolative behavior has never been observed. Thus, a question arises whether the analogous magnetic-field-controlled I-M transition (IMT) and domain percolation can be achieved in double-exchange cobaltites, and what is the
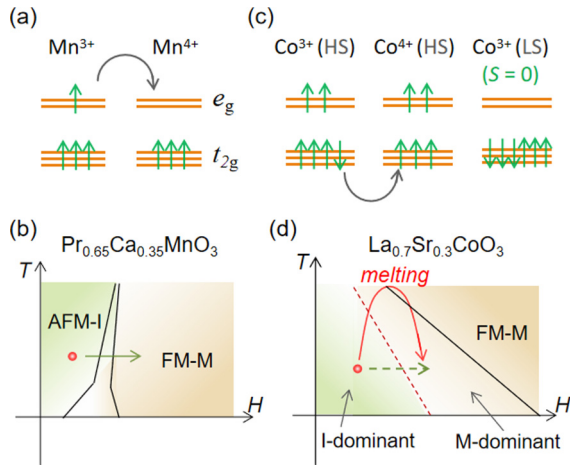
*meng.wang@riken.jp

FIG. 1. Comparison of the orbital configurations and phase diagrams of manganite and cobaltite. Schematics of the $d-$orbital occupancy and dominant double-exchange hopping mechanisms in (a) $Pr_{0.65}Ca_{0.35}MnO_3$ and (c) $La_{0.7}Sr_{0.3}CoO_3$. The coexistence of high-spin (HS) and low-spin (LS) of Co^{3+} and the double-exchange mechanism of $La_{0.7}Sr_{0.3}CoO_3$ are given in Refs. [13–16]. (b) Temperature- and magnetic-field-dependent $(T-H)$ phase diagram of $Pr_{0.65}Ca_{0.35}MnO_3$ from Ref. [12]. The antiferromagnetic-insulator (AFM-I) ground state can be tuned to a ferromagnetic-metal (FM-M) state with a magnetic field sweeping. (d) Schematic $T-H$ phase diagram of tensile-strained $La_{0.7}Sr_{0.3}CoO_3$. The ground state possesses coexisting non-FM insulating and FM-M phases, with more non-FM volume fraction, and behaves as an insulator in transport. Manipulation of the volume fraction of two phases with an isothermal magnetic field, as indicated by the dashed arrow, is difficult, while a kinetic pathway combining thermal activation and a magnetic field can effectively tune the volume fraction of two phases to realize an insulator-dominant (I-dominant) to metal-dominant (M-dominant) phase transition, as indicated by the red arrow.

physical origin that drives them differently from CMR manganites?

In this paper, we grow $La_{0.7}AE_{0.3}CoO_3$ films on $SrTiO_3$ substrate (i.e., $La_{0.7}AE_{0.3}CoO_3$/STO) with a tensile strain to stabilize weakly insulating phases (Fig. 2) [25] and study their magnetic response. By combining the transport, magnetiza-

tion, and magnetic force microscopy (MFM) measurements on $La_{0.7}Sr_{0.3}CoO_3$/STO, we visualize a submicrometer-scale phase separation state consisting of FM-M domains and non-FM-I domains. Moreover, we find that an isothermal field sweep has weak effects on tuning its resistance and domain profiles, while an isofield temperature sweep [i.e., field cooling (FC)] can dramatically enhance the degree of percolation of the FM domain and result in a crossoverlike IMT [as illustrated in Fig. 1(d)]. The contrasting behavior of the MR between the isothermal field sweep and FC processes suggests that a nonergodic feature is involved in the $La_{0.7}Sr_{0.3}CoO_3$/STO film, especially at low temperatures. Finally, by investigating the systematic change of the nonergodic properties with lattice and spin states from $La_{0.7}Ca_{0.3}CoO_3$, $La_{0.7}Sr_{0.3}CoO_3$, to $La_{0.7}Ba_{0.2}Sr_{0.1}CoO_3$, we find that $LS-Co^{3+}$ with quenched moment could be a main factor in inhibiting the domain percolation and suppressing the MR.

II. RESULTS AND DISCUSSION

We first show the resistance-temperature $(R-T)$ curves under various magnetic fields, which are applied along the out-of-plane (OOP) direction [Fig. 3(a)]. A main finding of this paper is that, while the transport property is weakly insulating at zero field, as reported [25], the $R-T$ curve at 14 T shows metallic temperature dependence, although a slight upturn can be seen <70 K. The MR at 14 T and the lowest temperature (3 K) amounts to $\approx -900\%$, one order of magnitude larger than previous reports in bulk materials [19–22]. On the other hand, no first-order transitionlike anomaly can be seen in the temperature dependence at each magnetic field. This observation is in stark contrast with CMR manganites, such as $Pr_{0.65}Ca_{0.35}MnO_3$ [12].

To gain more insight into the change from insulating to metallic ground states, we investigated how the resistance evolves under isothermal magnetic field sweep conditions at the lowest temperature 3 K. Field sweep experiments were performed, starting from either the zero-FC (ZFC) or 14T-FC states, and the results are shown in Fig. 3(b). Although the ZFC state exhibits a pronounced continuous decrease in resistance as the magnetic field increases, its resistance value
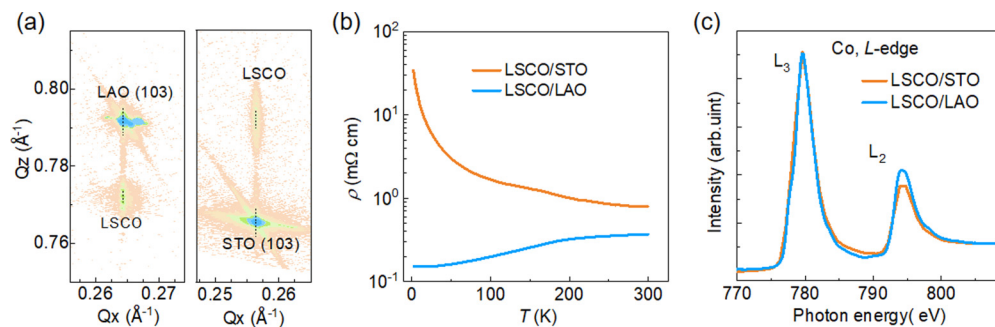

FIG. 2. Characteristics of the strained LSCO films with $x = 0.3$. (a) Reciprocal space mappings (RSMs) around the (103) diffraction peaks of the LSCO films grown on LAO (left) and STO (right). (b) $R-T$ curves of the two films with metallic behavior on LAO (blue) and insulating behavior on STO (orange). (c) x-ray absorption spectroscopy (XAS) of the LSCO films grown on STO and LAO measured around the cobalt L edge at room temperature. The suppression of the $Co-L_2$ peak intensity (i.e., increased L_3/L_2 ratio) in the LSCO/STO film distinctly indicates reduced low-spin and enhanced high-spin states by the tensile strain [34].
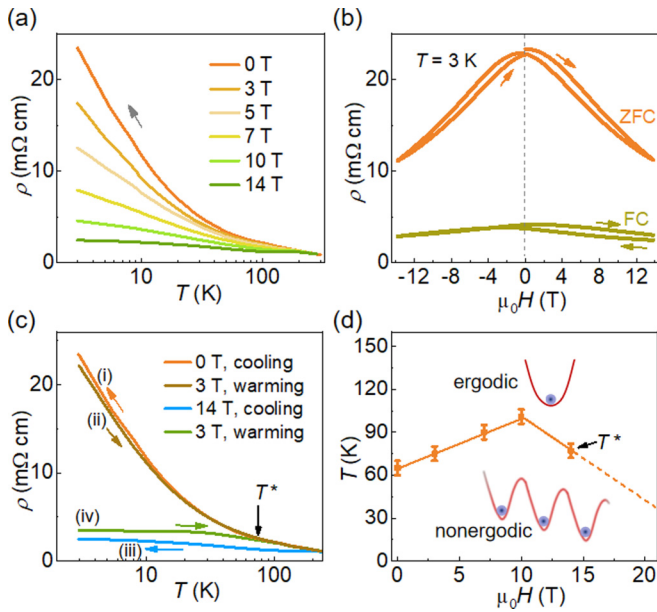
FIG. 3. Magnetic-field-controlled insulator-metal crossover and emergent nonergodic state in the $La_{0.7}Sr_{0.3}CoO_3$/STO film. (a) Temperature-dependent resistivity ($R-T$) curves measured with gradually increasing magnetic fields. All curves are measured with temperature cooling from 300 to 3 K. (b) Magnetic-field-dependent resistance curves measured at 3 K after undergoing zero-field-cooling (ZFC) and a 14 T field-cooling (FC) processes. Arrows indicate magnetic field sweeping. (c) $R-T$ curves measured with different histories. The arrows indicate the measuring pathways: (i) cooling from 250 to 3 K with zero field, (ii) tuning the magnetic field to 3 T and warming from 3 to 250 K with the magnetic field, (iii) cooling from 250 to 3 K at 14 T, and (iv) decreasing the magnetic field to 3 T at 3 K and finally warming up to 250 K. The merging of curves (ii) and (iv) indicates the characteristic temperature (T^*) that separates the ergodic (path-independent) and nonergodic (path-dependent) regimes. (d) Ergodic and nonergodic phase diagram within the $T-H$ plane. The characteristic temperatures are obtained by a variety of transport measurements, as shown in (c) and Figs. 4 and 6(e). Insets illustrate the single-well and multiwell states in two regimes. The dashed line denotes the tendency toward a higher magnetic field. Magnetic field is normal to the film.

at 14 T does not become as low as that of the 14T-FC state. Moreover, when the magnetic field is decreased from 14 T to zero, the resistance of the ZFC state reverts to a high value close to that of the initial state, whereas the resistance of the 14T-FC state remains a low value. Thus, compared with the isothermal field sweep after ZFC, FC from high temperatures works more effectively for controlling the ground state.

The temperature/field history-dependent transport properties clearly indicate that the system at low temperatures is in a nonergodic state [6,26,27]. In such a context, a phenomenological complex free-energy landscape with multiple minima is often considered. Below a characteristic temperature T^*, the system can be trapped in different local minima depending on the thermodynamic path, giving rise to history-dependent macroscopic physical properties. To characterize the nonergodic physical properties of $La_{0.7}Sr_{0.3}CoO_3$/STO, we define

T^*, below which the $R-T$ curve depends on the thermodynamic path. Figure 3(c) illustrates the determination of T^*, for instance, at 3 T (regarding other magnetic fields, see Fig. 4). The sample was first cooled to 3 K at either zero field [process (i); ZFC] or 14 T [process (iii); 14T-FC]; then the magnetic field was increased or decreased to a prescribed field 3 T; and finally, the $R-T$ curve was measured in the heating process at the prescribed field [process (ii) or (iv)]. While the two obtained $R-T$ curves [process (ii) or (iv)] are well separated at low temperatures, they eventually merge at T^*, above which the physical properties are independent of the thermodynamic path. Thus, we obtained the magnetic field dependence of T^*, as summarized in Fig. 3(d). Clearly, in the present magnetic field range, the ground-state properties invariably belong to the nonergodic regime.

Given the strong coupling between electronic states and magnetic orders in double-exchange manganese oxides, we also investigated the magnetic-field-driven phase evolution in terms of the magnetization measurements. Our $La_{0.7}Sr_{0.3}CoO_3$/STO film exhibits a FM transition with a Curie temperature (T_c) ≈ 200 K, which is clearly observed when the external magnetic field is applied along the in-plane (IP) direction [Fig. 5(a)]. A sharp magnetization-reversal transition is also observed in the IP direction, qualitatively consistent with previous reports [25]. The comparison of magnetic-field-dependent magnetization ($M-H$) curves at 10 K with the magnetic fields along the IP and OOP directions [Fig. 5(a), inset] and the angle-dependent resistance measured with the $La_{0.7}Sr_{0.3}CoO_3$/STO film rotating from 0° to 360° [Fig. 4(c)] indicates that the magnetic easy axis is closer to IP. As in the case of the transport measurements (Fig. 3), here, we also performed the magnetization measurements under ZFC and FC with an OOP magnetic field, and the $M-H$ curves for each cooling condition are shown in Fig. 5(b). Interestingly, the 7T-FC state exhibits a larger magnetic moment (0.73 μ_B per u.c.) than the case in which 7 T is applied after a ZFC process (0.68 μ_B per u.c.), showing an increase of 7%. These observations imply the insulating $La_{0.7}Sr_{0.3}CoO_3$/STO film is in a phase-mixed state consisting of the FM and non-FM (or AFM) domains with a FC-induced percolation.

To substantiate the possible phase separation in the $La_{0.7}Sr_{0.3}CoO_3$/STO film and gain more insight into the phase evolution, we performed a series of MFM measurements at 10 K for both the ZFC and FC states (see Methods). Figures 5(c)–5(g) display the MFM images recorded at different magnetic fields for the ZFC and FC states, and the topography image measured at the same position is shown in Fig. 5(h). The areas with relatively large negative frequency shifts (Δf) are ascribed to the FM phase (orange), whereas the areas with positive or near zero frequency shifts are ascribed to the non-FM (or AFM) phase (olive) [28–31], which have no response to the increase of the magnetic field [as indicated by black arrows in Figs. 5(e) and 5(f)]. Here, two aspects can be highlighted. First, as expected, a magnetically inhomogeneous state with a submicrometer scale is found for both FC and ZFC states, which is robust even at 7 T, substantiating the phase-separation scenario deduced from the macroscopic transport and magnetization measurements. Second, while the FM-M domains are mostly isolated from each other in the ZFC state at 7 T, they tend to expand and
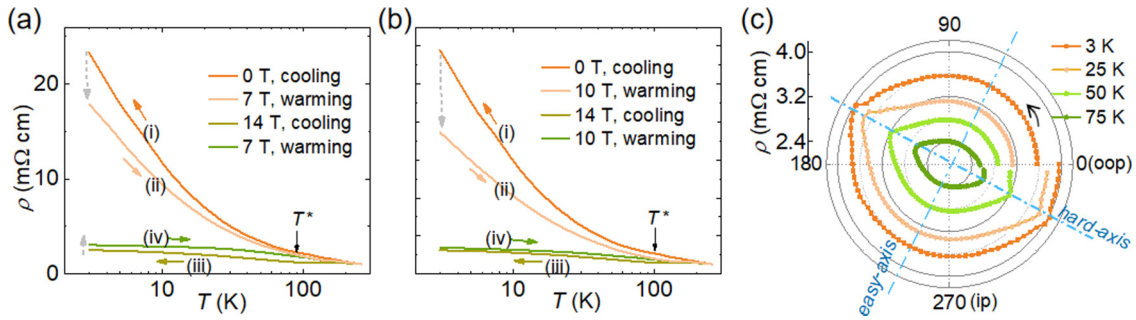
FIG. 4. Magnetic transport properties in the $La_{0.7}Sr_{0.3}CoO_3$/STO film. (a) and (b) $R-T$ curves measured with different histories in the $La_{0.7}Sr_{0.3}CoO_3$/STO film. The arrows indicate the measuring pathways: (i) cooling from 250 to 3 K at zero field, (ii) tuning the magnetic field to (a) 7 T and (b) 10 T at 3 K and warming from 3 to 250 K at the magnetic field, (iii) cooling from 250 to 3 K at 14 T, and (iv) decreasing the magnetic field to (a) 7 T and (b) 10 T at 3 K and finally warming it up to 250 K. T^* indicates the characteristic temperature needed to separate the ergodic and nonergodic regions. (c) Angle-dependent resistance measured with the $La_{0.7}Sr_{0.3}CoO_3$/STO film rotating from 0° to 360° at a magnetic field of 14 T. Blue dashed lines indicate the magnetic hard axis (maximum resistance) and easy axis (minimum resistance) [41].

connect with neighboring FM-M domains in the 7T-FC state, as marked by circles in Figs. 5(e) and 5(f). These observations indicate that the increase in the volume fraction of the FM-M phases and the history-dependent domain connection play a crucial role in stabilizing the low-resistance state, rationalizing the nonergodic transport behavior. Note that, although the electronic phase separation has been proposed in bulk LSCO materials [23,24], the domain percolation under thermal and

magnetic field stimuli has never been reported. Considering that our thin film material shows one order of magnitude larger MR than previous reports in bulk cobaltites [19–22], the field-induced percolation should be more difficult to detect in bulk.

We have established that, compared with manganites, the magnetic-field-controlled percolation of the FM-M domains in $La_{0.7}Sr_{0.3}CoO_3$/STO is dramatically suppressed. This observation indicates that, although domain wall pinning exists

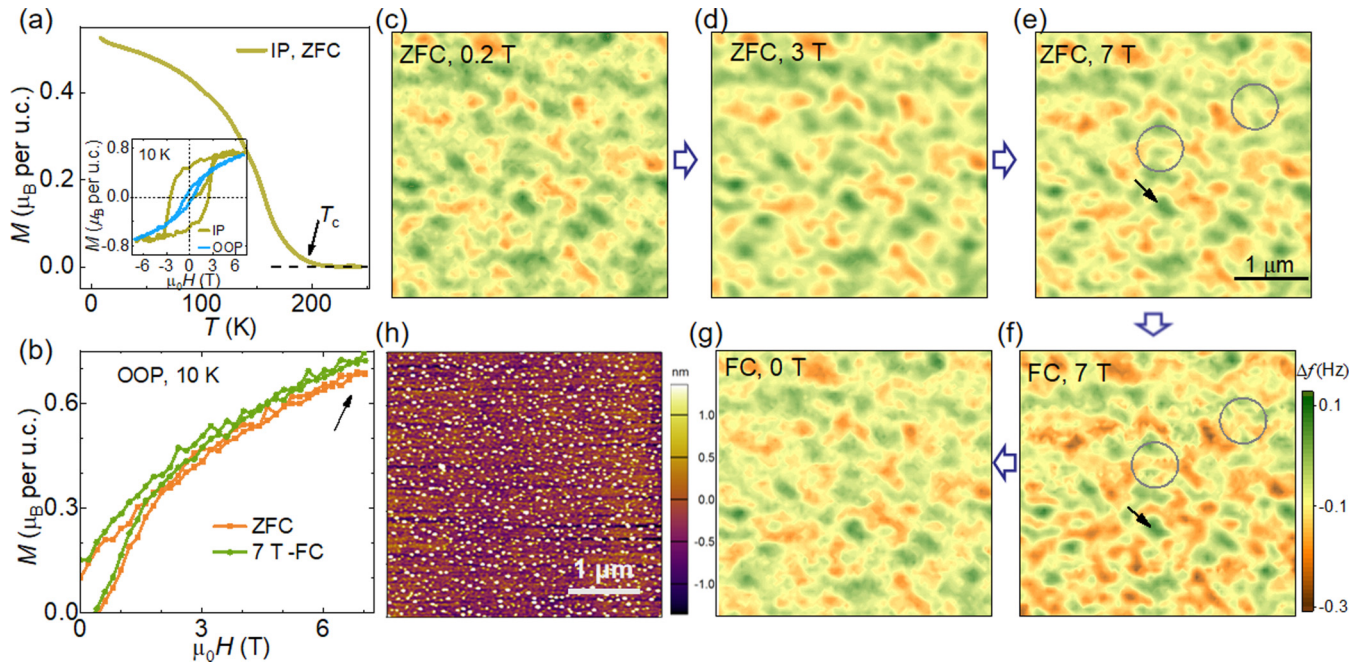FIG. 5. Comparison of the magnetic properties of different states in $La_{0.7}Sr_{0.3}CoO_3$/STO film. (a) Magnetization with temperature dependence ($M-T$) measured with an in-plane (IP) magnetic field. Inset: Comparison of the field-dependent magnetization ($M-H$) curves (10 K) with magnetic fields along the IP and out-of-plane (OOP) directions. The $M-T$ curve is measured after the $M-H$ loop and with a field of 0.2 T IP. (b) $M-H$ curves measured with the field applied OOP after undergoing zero-field-cooling (ZFC) and a 7 T field-cooling (FC) process, respectively. The magnetization at 7 T in the FC state (0.73 μ_B per u.c.) increases $\sim 7\%$ compared with that in the ZFC state (0.68 μ_B per u.c.), as indicated by the arrow. Magnetic force microscopy (MFM) images measured at 10 K after undergoing ZFC at (c) 0.2 T, (d) 3 T, (e) 7 T, and after 7T-FC process at (f) 7 T and (g) 0 T. Magnetic field is OOP. The response from the orange area is enhanced at high magnetic fields, corresponding to a ferromagnetic (FM) domain flipping from near IP to OOP by the increased magnetic field. The black arrows indicate the area with no response to the magnetic field and imply a non-FM domain, and the circles highlight the percolation of FM domains in (e) and (f). (h) Topography image of the MFM-studied sample measured at the same location, in which the roughness shows no relationship to the magnetic domain profile.
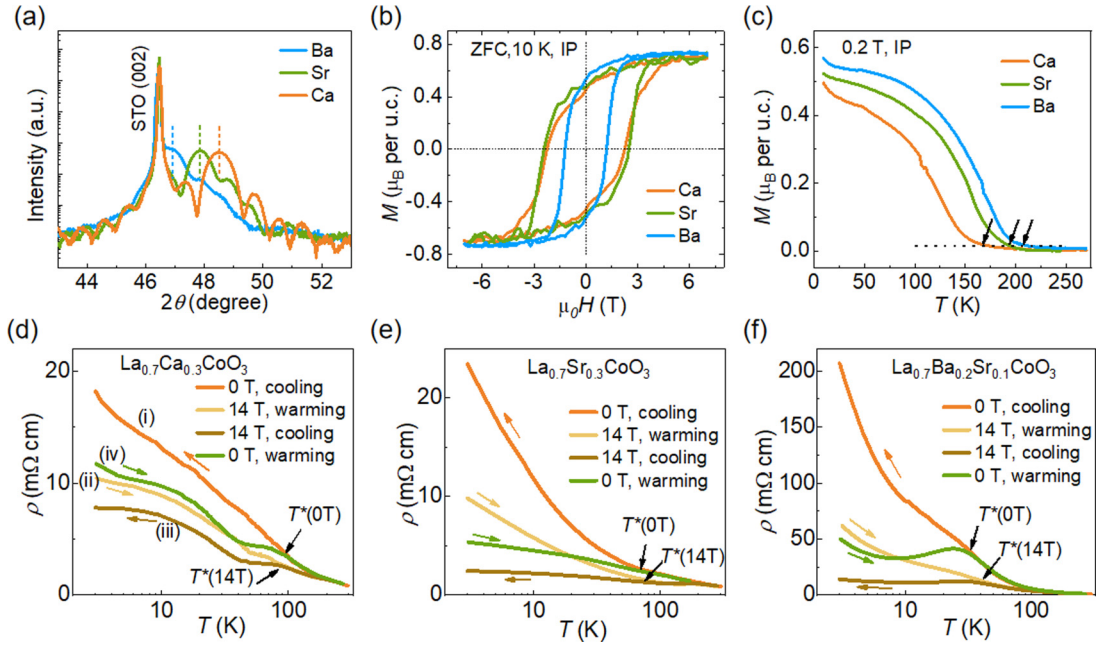
FIG. 6. Comparison of the magnetic responses among $La_{0.7}AE_{0.3}CoO_3$/STO films. (a) X-ray diffraction $2\theta-\omega$ scans near the (002) diffraction peaks of the $La_{0.7}Ca_{0.3}CoO_3$ (Ca), $La_{0.7}Sr_{0.3}CoO_3$ (Sr), and $La_{0.7}Ba_{0.2}Sr_{0.1}CoO_3$ (Ba) films grown on STO. (b) $M-H$ and (c) $M-T$ curves of the three films with magnetic field in-plane (IP). The $M-T$ curves are measured following the $M-H$ measurements with a magnetic field at 0.2 T. Arrows in (c) indicate the T_c, which increases with the expanded c axis. (d)–(f) $R-T$ curves measured with different histories in three films. The color arrows indicate the measuring pathways. T^* (0 T) and T^* (14 T) denote the characteristic temperatures that separate the ergodic (high-temperature) and nonergodic (low-temperature) regimes at zero field and 14 T, respectively. From Ca, Sr, to Ba, the enhanced A-site mismatch and expanded lattice induce a gradually increasing resistivity. However, the T^* tends to decrease while the magnetoresistance (MR) tends to increase, both of which indicate a suppressed nonergodic behavior.

in manganites [31], a much stronger pinning effect is involved in $La_{0.7}Sr_{0.3}CoO_3$/STO. To get further insight into the physical origin, we compare the magnetic and transport properties among $La_{0.7}AE_{0.3}CoO_3$/STO films with changing the A-site doping elements from Ca, Sr, to Ba (Fig. 6). The three films possess identical doping level and IP lattice symmetry, while expanding the OOP lattice [Fig. 6(a)]. The $M-H$ [Fig. 6(b)] and $M-T$ [Fig. 6(c)] measurements indicate that the three films have similar magnetic properties with slightly different T_c. Interestingly, nonergodic transport behavior is observed in all compounds, while they tend to decreased characteristic temperatures at both zero field and 14 T from Ca, Sr, to Ba, as shown in Figs. 6(d)–6(f), which suggests a gradually reduced barrier for domain wall motion.

As an origin of the domain wall pinning, we first consider local lattice distortion due to the difference of the ionic radius between La^{3+} and AE^{2+} in the A sites. Referring to previous studies on manganites, the magnitude of the quenched disorder arising from a solid solution can be characterized by the variance of the ionic radii $\sigma^2 = \sum x_i (r_i - r_A)^2$, where x_i and r_i are the fractional occupancies and the ionic radius of La^{3+} or AE^{2+}, respectively, and r_A is the average radius of

A-site ions [32]. According to this value (Tables I and II), the magnitude of the quenched disorder (and thus T^*) is expected to increase from Ca, Sr, to Ba. Obviously, this tendency is opposite to the experimental observations, leading us to consider another mechanism for domain wall pinning.

We then consider the LS-state Co^{3+} ions as a potential factor. In contrast to manganites that only host HS-state Mn ions [11], the LS-state Co^{3+} ions can be mixed with HS-state ions in cobaltites [14]. Because the LS-state Co^{3+} ions have no spin moment ($S = 0$) [Fig. 1(c)], they are expected to cut the network of the magnetic interaction and thus inhibit the evolution of the FM-M domains, which is accompanied by the change of magnetism. To examine this scenario, we performed x-ray absorption spectroscopy (XAS) on cobalt L edges and oxygen K edges. We find that, with changing A-site dopants from Ca, Sr, to Ba, the L_3/L_2 absorption ratio increases [Fig. 7(a)], while the pre-absorption peaks of oxygen K edges are suppressed gradually [Fig. 7(b)]. These results indicate that the number of HS-state Co sites increases from Ca, Sr, to Ba with lattice expansion, at the expense of the LS-state Co sites [33–35]. The increased HS-state Co sites also reasonably account for the increase of the FM transition temperature

TABLE I. Ionic radii in the $La_{0.7}AE_{0.3}CoO_3$ materials.

Cation	La^{3+}	Ca^{2+}	Sr^{2+}	Ba^{2+}	Co^{3+}(HS)	Co^{3+}(LS)	Co^{4+}(HS)	O^{2-}
Radius (Å)	1.216	1.179	1.31	1.47	0.61	0.545	0.53	1.4

TABLE II. Variance of the A-site ionic radii [32].

Materials	$La_{0.7}Ca_{0.3}CoO_3$	$La_{0.7}Sr_{0.3}CoO_3$	$La_{0.7}Ba_{02}Sr_{0.1}CoO_3$
σ^2	0.00029	0.00186	0.01016

[Figs. 6(b), 6(c), and 7(c)]. These observations are consistent with our scenario that the LS-state Co sites tend to inhibit the domain wall motion and thus form an energy barrier for it: From Ca, Sr, to Ba, the ratio of LS-state Co^{3+} sites decreases, resulting in a weaker pinning of the domain wall and thus decreased T^* [Fig. 7(c)]. These results also explain why the MR is relatively small in bulk $La_{0.7}Sr_{0.3}CoO_3$. The previous study revealed that the LS- to HS-state transition is facilitated by the expansion of the unit cell volume because $HS-Co^{3+}$ naturally needs larger local volume than the LS one [33,36–38]. When the bulk $La_{0.7}Sr_{0.3}CoO_3$ and $La_{0.7}AE_{0.3}CoO_3$/STO films are compared with respect to the unit-cell volume (Table III) [39], the bulk is found to have a smaller lattice volume, indicating denser LS states. Thus, the comparison between the bulk and thin films also suggests a key role of the LS-state Co^{3+} sites in pinning the domain walls.

III. SUMMARY AND CONCLUSIONS

In summary, here, we observe a magnetic-field-controlled I-M crossover with a thermally activated domain percolation in cobaltites. The systematic studies of magnetic and transport properties with a dependence on spin state reveal the mixed LS sites as a key factor in pinning the domain wall and enhancing the energy barrier for the magnetic-field-controlled phase evolution in cobaltite systems. These results demonstrate that the spin-state degree of freedom inherent to cobaltite systems can give rise to a domain wall pinning center and make the IMT under isothermal field sweep difficult. In contrast, mixed-valent perovskite manganites have no spin-state degree of freedom (all Mn sites are in HS state), and thus, the magnetic-field-induced phase evolution is more feasible. Thus, the presence/absence of the spin-state degree of freedom is crucial in considering the magnetotransport properties of a double-exchange system near the IMT.
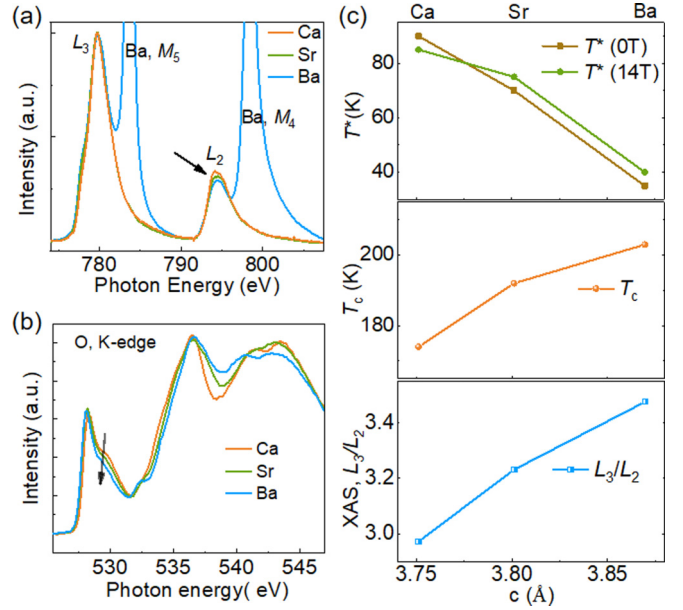
FIG. 7. Comparison of the nonergodic properties and spin states among various compounds. Normalized x-ray absorption spectroscopy (XAS) around (a) cobalt L edges and (b) oxygen K edges, obtained from $La_{0.7}Ca_{0.3}CoO_3$ (Ca), $La_{0.7}Sr_{0.3}CoO_3$ (Sr), and $La_{0.7}Ba_{0.2}Sr_{0.1}CoO_3$ (Ba) films at 90 K. Arrows highlight the reduced intensity of L_2 peaks and pre-absorption of oxygen K edges from Ca, Sr, to Ba. (c) Summary of the nonergodic characteristic temperature (T^*) at zero field and 14 T, Curie temperature (T_c), and the ratio of L_3 and L_2 peak intensity in XAS, with a dependence on the doping elements and out-of-plane lattice constant c. T_c and T^* are obtained from Fig. 6.

APPENDIX

1. Thin-film growth and x-ray diffraction

The films were epitaxially grown on STO and $LaAlO_3$ (LAO) substrates by a pulsed laser deposition method. The stoichiometric targets were fabricated with La_2O_3, $SrCO_3$, $BaCO_3$, $CaCO_3$, and Co_3O_4 powders mixed and sintered at $1000\,°C$. During sample growth, the substrate temperature was kept at $560\,°C$, and the oxygen partial pressure was kept at 100 mTorr. The laser fluence was $2.0\,J/cm^2$ (KrF, $\lambda = 248$ nm), and the deposition frequency was 5 Hz. After deposition was finished, the samples were cooled to room temperature at a rate of $10\,°C/min$ under an oxygen pressure of 10 Torr. After that, the samples were moved to an ozone furnace and annealed at $260\,°C$ for 45 min to reduce the oxygen vacancies. Note that Co^{4+} is chemically unstable and that oxygen vacancies form easily [40], especially for films grown with tensile strains, which will give rise to a much larger resistivity. Thus, to fabricate high-quality films, we had to grow films under high oxygen pressure, followed by

TABLE III. Unit cell volumes of $La_{0.7}AE_{0.3}CoO_3$/STO films obtained from x-ray diffraction with a comparison with bulk $La_{0.7}Sr_{0.3}CoO_3$.

Types	Bulk [39]	Films grown on STO		
Materials	$La_{0.7}Sr_{0.3}CoO_3$	$La_{0.7}Ca_{0.3}CoO_3$	$La_{0.7}Sr_{0.3}CoO_3$	$La_{0.7}Ba_{02}Sr_{0.1}CoO_3$
Volume ($Å^3$)	56.40	57.18	57.94	59.01

an ozone annealing process. X-ray diffraction measurements were performed using a high-resolution diffractometer (PANalytical) with monochromatic Cu K_{α_1} ($\lambda = 1.5406$ Å) x rays.

2. Transport and magnetization measurements

Because oxygen vacancies are very easily formed by the deposition of electrodes, the resistance was measured with four probe geometries using indium to directly contact the gold wires with the samples (2 × 3.5 mm). A PPMS system (Quantum Design) was used with a magnetic field limit of 14 T, and all resistances except the angle dependence were measured with the magnetic field along the normal direction. The magnetic moments were measured using an MPMS system (Quantum Design) with a magnetic field limit of 7 T. All measurements were performed with fresh samples annealed in ozone.

3. MFM image measurement

Frequency-modulated MFM measurements were carried out with a commercially available scanning probe microscope (attocube AFM/MFM I). An MFMR tip (supplied by NANOSENSORS) with a tip radius of ∼50 nm and a coercive field of 0.1 T was used. MFM scanning was performed in noncontact mode with a lift height of 100 nm. The scan rate and the step width were set to 1 μm/s and 50 nm, respectively. The MFM images were first measured at 10 K and different magnetic fields from a ZFC process, after which the sample was warmed up to 120 K (due to the constraint of the measurement system) and cooled back to 10 K at 7 T, and then the images were recorded again for the FC state.

4. XAS measurement

The soft XAS were measured in BL14, Hiroshima Synchrotron Radiation Center (HiSOR), Hiroshima University, Japan. The data were collected through a total electron yield mode. All spectra were shifted to be zero at the pre-absorption region and then normalized to have an identical value at the end of the absorption edges, for comparison among different curves.

[1] E. Dagotto, Science **309**, 257 (2005).

[2] M. Imada, A. Fujimori, and Y. Tokura, Rev. Mod. Phys. **70**, 1039 (1998).

[3] A. Moreo, S. Yunoki, and E. Dagotto, Science **283**, 2034 (1999).

[4] K. H. Ahn, T. Lookman, and A. R. Bishop, Nature (London) **428**, 401 (2004).

[5] M. Uehara, S. Mori, C. H. Chen, and S.-W. Cheong, Nature (London) **399**, 560 (1999).

[6] W. Wu, C. Israel, N. Hur, S. Park, S.-W. Cheong, and A. de Lozanne, Nat. Mater. **5**, 881 (2006).

[7] S. S. Hong, M. Gu, M. Verma, V. Harbola, B. Y. Wang, D. Lu, A. Vailionis, Y. Hikita, R. Pentcheva, J. M. Rondinelli *et al.*, Science **368**, 71 (2020).

[8] T. Miao, L. Deng, W. Yang, J. Ni, C. Zheng, J. Etheridge, S. Wang, H. Liu, H. Lin, Y. Yu *et al.*, Proc. Natl. Acad. Sci. USA **117**, 7090 (2020).

[9] E. Dagotto, T. Hotta, and A. Moreo, Phys. Rep. **344**, 1 (2001).

[10] E. Dagotto, New J. Phys. **7**, 67 (2005).

[11] A.-M. Haghiri-Gosnet and J.-P. Renard, J. Phys. D: Appl. Phys. **36**, R127 (2003).

[12] Y. Tomioka, A. Asamitsu, H. Kuwahara, Y. Moritomo, and Y. Tokura, Phys. Rev. B **53**, R1689 (1996).

[13] P. Augustinský, V. Křápek, and J. Kuneš, Phys. Rev. Lett. **110**, 267204 (2013).

[14] M. Merz, P. Nagel, C. Pinta, A. Samartsev, H. v. Löhneysen, M. Wissinger, S. Uebe, A. Assmann, D. Fuchs, and S. Schuppler, Phys. Rev. B **82**, 174416 (2010).

[15] P. Friš, D. Munzar, O. Caha, and A. Dubroka, Phys. Rev. B **97**, 045137 (2018).

[16] D. Fuchs, M. Merz, P. Nagel, R. Schneider, S. Schuppler, and H. von Löhneysen, Phys. Rev. Lett. **111**, 257203 (2013).

[17] M. Kriener, C. Zobel, A. Reichl, J. Baier, M. Cwik, K. Berggold, H. Kierspel, O. Zabara, A. Freimuth, and T. Lorenz, Phys. Rev. B **69**, 094417 (2004).

[18] R. Caciuffo, D. Rinaldi, G. Barucca, J. Mira, J. Rivas, M. A. Señarís-Rodríguez, P. G. Radaelli, D. Fiorani, and J. B. Goodenough, Phys. Rev. B **59**, 1068 (1999).

[19] M. A. Señarís-Rodríguez and J. B. Goodenough, J. Solid State Chem. **118**, 323 (1995).

[20] R. Mahendiran, A. K. Raychaudhuri, A. Chainani, and D. D. Sarma, J. Phys.: Condens. Matter **7**, L561 (1995).

[21] D. Louca and J. L. Sarrao, Phys. Rev. Lett. **91**, 155501 (2003).

[22] J. Wu and C. Leighton, Phys. Rev. B. **67**, 174408 (2003).

[23] P. L. Kuhns, M. J. R. Hoch, W. G. Moulton, A. P. Reyes, J. Wu, and C. Leighton, Phys. Rev. Lett. **91**, 127202 (2003).

[24] D. Phelan, D. Louca, K. Kamazawa, S.-H. Lee, S. N. Ancona, S. Rosenkranz, Y. Motome, M. F. Hundley, J. F. Mitchell, and Y. Moritomo, Phys. Rev. Lett. **97**, 235501 (2006).

[25] A. D. Rata, A. Herklotz, K. Nenkov, L. Schultz, and K. Dörr, Phys. Rev. Lett. **100**, 076401 (2008).

[26] M. K. Chattopadhyay, S. B. Roy, and P. Chaddah, Phys. Rev. B **72**, 180401(R) (2005).

[27] S. Scherg, T. Kohlert, P. Sala, F. Pollmann, B. H. Madhusudhana, I. Bloch, and M. Aidelsburger, Nat. Commun. **12**, 4490 (2021).

[28] P. M. Sass, W. Ge, J. Yan, D. Obeysekera, J. J. Yang, and W. Wu, Nano Lett. **20**, 2609 (2020).

[29] K. Matsuura, H. Oike, V. Kocsis, T. Sato, Y. Tomioka, Y. Kaneko, M. Nakamura, Y. Taguchi, M. Kawasaki, Y. Tokura *et al.*, Phys. Rev. B **103**, L041106 (2021).

[30] Q. Feng, D. Meng, H. Zhou, G. Liang, Z. Cui, H. Huang, J. Wang, J. Guo, C. Ma, X. Zhai *et al.*, Phys. Rev. Mater. **3**, 074406 (2019).

[31] H. Zhou, L. Wang, Y. Hou, Z. Huang, Q. Lu, and W. Wu, Nat. Commun. **6**, 8980 (2015).

[32] Y. Tomioka and Y. Tokura, Phys. Rev. B **70**, 014432 (2004).

[33] P. G. Radaelli and S.-W. Cheong, Phys. Rev. B **66**, 094408 (2002).

[34] M. W. Haverkort, Z. Hu, J. C. Cezar, T. Burnus, H. Hartmann, M. Reuther, C. Zobel, T. Lorenz, A. Tanaka, N. B. Brookes *et al.*, Phys. Rev. Lett. **97**, 176405 (2006).

[35] R. F. Klie, J. C. Zheng, Y. Zhu, M. Varela, J. Wu, and C. Leighton, Phys. Rev. Lett. **99**, 047203 (2007).

[36] H. Seo, A. Posadas, and A. A. Demkov, Phys. Rev. B **86**, 014430 (2012).

[37] A. D. Rata, A. Herklotz, L. Schultz, and K. Dörr, Eur. Phys. J. B **76**, 215 (2010).

[38] Y. Yokoyama, Y. Yokoyama, Y. Yamasaki, M. Taguchi, Y. Hirata, K. Takubo, J. Miyawaki, Y. Harada, D. Asakura, J. Fujioka *et al.*, Phys. Rev. Lett. **120**, 206402 (2018).

[39] A. N. Petrov, O. F. Kononchuka, A. V. Andreeva, V. A. Cherepanova, and P. Kofstadb, Solid State Ionics **80**, 189 (1995).

[40] Y. Wang, Q. He, W. Ming, M.-H. Du, N. Lu, C. Cafolla, J. Fujioka, Q. Zhang, D. Zhang, S. Shen *et al.*, Phys. Rev. X **10**, 021030 (2020).

[41] G. Koster, L. Klein, W. Siemons, G. Rijnders, J. S. Dodge, C.-B. Eom, D. H. A. Blank, and M. R. Beasley, Rev. Mod. Phys. **84**, 253 (2012).